Spring 2015

Preparation of bismuth telluride based thermoelectric nanomaterials via low-energy ball milling and their property characterizations

Christopher Robinson
Purdue University

Follow this and additional works at: https://docs.lib.purdue.edu/open_access_theses

 Part of the Nanoscience and Nanotechnology Commons

Recommended Citation

Robinson, Christopher, "Preparation of bismuth telluride based thermoelectric nanomaterials via low-energy ball milling and their property characterizations" (2015). *Open Access Theses*. 601.
https://docs.lib.purdue.edu/open_access_theses/601

PURDUE UNIVERSITY
GRADUATE SCHOOL
Thesis/Dissertation Acceptance

This is to certify that the thesis/dissertation prepared

By Christopher A. Robinson

Entitled
PREPARATION OF BISMUTH TELLURIDE BASED THERMOELECTRIC NANOMATERIALS VIA LOW-ENERGY
BALL MILLING AND THEIR PROPERTY CHARACTERIZATIONS

For the degree of Master of Science in Mechanical Engineering

Is approved by the final examining committee:

Xiulin Ruan
_____
Chair

Amy Marconnet

Xianfan Xu

To the best of my knowledge and as understood by the student in the Thesis/Dissertation Agreement, Publication Delay, and Certification Disclaimer (Graduate School Form 32), this thesis/dissertation adheres to the provisions of Purdue University's "Policy of Integrity in Research" and the use of copyright material.

Approved by Major Professor(s): Xiulin Ruan

Approved by: Ganesh Subbarayan   4/24/2015
                Head of the Departmental Graduate Program   Date

PREPARATION OF BISMUTH TELLURIDE BASED THERMOELECTRIC NANOMATERIALS VIA

LOW-ENERGY BALL MILLING AND THEIR PROPERTY CHARACTERIZATIONS

A Thesis

Submitted to the Faculty

of

Purdue University

by

Christopher A. Robinson

In Partial Fulfillment of the

Requirements for the Degree

of

Master of Science in Mechanical Engineering

May 2015

Purdue University

West Lafayette, Indiana

ACKNOWLEDGEMENTS

There are many people that I would like to thank that have made my education at Purdue such a success. First and foremost, I must thank my wife and family who have supported me at every step of my education and given me confidence in myself. I would also like to thank my advisor, Dr. Xiulin Ruan, for his support and guidance in this research area. It was Dr. Ruan who offered me a position as an undergraduate research assistant that has fostered my interest in the areas of heat transfer and nanotechnology. I would also like to thank Dr. Amy Marconnet and Dr. Xianfan Xu for taking time to be a part of my advisory committee and supporting me education.

I have also benefitted from assistance from many other students I have worked with during my time at Purdue. I would like to thank Dr. Liangliang Chen for his guidance and thoughtful discussions as my mentor during my time as an undergraduate researcher. I would also like to thank Kelly Rickey for her assistance with many of the characterization techniques I have utilized in this work. I am grateful for the assistance of Denny Hu and Kunal Thacker for their support in measuring thermal properties using the IR camera setup in Dr. Marconnet's lab.

TABLE OF CONTENTS

LIST OF FIGURES

LIST OF ABBREVIATIONS

ZT:	Dimensionless figure of merit
S:	Seebeck Coefficient
σ:	Electrical Conductivity
κ:	Thermal Conductivity
T:	Temperature
L:	Average Particle Diameter
K:	Shape Factor for XRD
λ:	X-ray Wavelength
β:	Width of the Diffraction Peak
SEM/TEM:	Scanning/Transmission Electron Microscopy
C:	Elementary Unit of Charge
K_B:	Boltzmann's Constant
m^*:	Effective Mass
n:	Carrier Concentration
Ra:	Rayleigh Number
Pr:	Prandtl Number
Nu:	Nusselt Number
h:	Convection Coefficient

ABSTRACT

Robinson, Christopher A., M.S.M.E., Purdue University, May 2015. Preparation of Bismuth Telluride Based Thermoelectric Nanomaterials Via Low-Energy Ball Milling and their Property Characterizations. Major Professor: Xiulin Ruan, School of Mechanical Engineering.

Thermoelectric materials are able to convert energy between heat and electricity with no moving parts, making them very appealing for power generation purposes. This is particularly appealing since many forms of energy generation lose energy to waste heat. The Livermore National Laboratory estimates that up to 55% of the energy created in traditional power plants is lost through heat generation [1]. As greenhouse gas emissions become a more important issue, large sources of waste like this will need to be harnessed.

Adoption of these materials has been limited due to the cost and efficiency of current technology. Bismuth telluride based alloys have a dimensionless figure of merit, a measure of efficiency, near one at room temperature, which makes it the best current material. In order to compete with other forms of energy generation, this needs to be increased to three or higher [2]. Recently, improvements in performance have come in the form of random nanostructured materials [3]. Bulk bismuth telluride is subjected to particle size reduction via high-energy ball milling in order to scatter phonons between

grains. This reduces the lattice thermal conductivity which in turn increases the performance of the material.

In this work, we investigate the use of low-energy ball milling as a method of creating nanoparticles of n-type and p-type Bi_2Te_3 alloys for thermoelectric applications. Optimization of parameters such as milling containers, milling media, contamination and milling time has resulted in creating 15nm particles of bismuth telluride alloys. After creating solid pellets of the resulting powders via hot pressing, the material's thermal and electrical conductivities as well as Seebeck coefficients were measured. The ZT of n-type $Bi_2Te_{2.7}Se_3$ created using this method is 0.32, while the p-type $Bi_{0.5}Sb_{1.5}Te_3$ exhibits a higher ZT of 1.24, both at room temperature.

CHAPTER 1.   INTRODUCTION

1.1   Motivation

Reducing greenhouse gas emissions is a critical issue to this generation of

scientists and engineers, driving research into forms of alternative energy. One

promising solution to this problem is to capture waste heat using thermoelectricity.

Thermoelectric materials are able to create a voltage difference when a temperature

differential is applied to each end of the material, via the Seebeck effect, and vice versa

via the Peltier effect. This type of conversion is particularly attractive since heat is an

abundant source of energy. Power plants typically operate at 30-40% efficiency, losing

upwards of 55% of its potential energy as waste heat, according to the Lawrence

Livermore National Laboratory, which is a large untapped source of energy [1].

There are some limitations to the widespread adoption of thermoelectrics,

mainly cost and performance. In today's market, thermoelectrics need to achieve a

dimensionless figure of merit (ZT), a measure of efficiency, upwards of three to compete

with other forms of power generation [2]. Bismuth telluride based alloys offer the most

competitive performance at room temperature with a ZT of about 1. Although the

efficiency can't quite rival other forms of energy generation, thermoelectrics have the

advantage of quiet and reliable operation since they have no moving parts.

Thermoelectric materials can be used to both create power from an existing heat source or used to cool a hot object. Car companies have looked toward thermoelectric generators in order to recover some heat lost through a vehicle's exhaust, lessening the load on the alternator and improving fuel economy [4]. Food and beverage coolers have utilized thermoelectrics in order to keep items cold without the use of ice. Many space missions, including the Mars rover, utilize radioisotope thermoelectric generators. These generators utilize the radiation emitted from a radioactive isotope in order to heat on side of the material, providing reliable energy for the missions [5].

1.2   Thermoelectric Modules

To make thermoelectric materials usable, a device must be made that is typically referred to as a thermoelectric module. A basic diagram of this module is shown in figure 1.1.
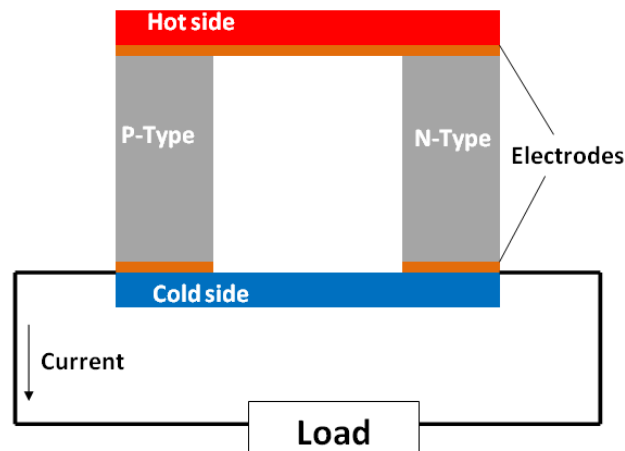
Figure 1.1. Diagram of a thermoelectric module.

In the n-type material, electrons flow from the hot side to the cold side, while in the p-type material holes flow from the hot side to the cold side. This means the thermoelectric effect of the individual n-type and p-type portions are summed for the total effect. Most thermoelectric modules consist of an array of n-type and p-type materials with each small element in the array referred to as a thermocouple [6]. This is common for most modules available for commercial purpose including those available through companies such as Laird and Ferrotec.

1.3   Previous Studies on Ball Milling Thermoelectrics

As previously discussed, ZT is a measure of the efficiency of thermoelectric materials, which is calculated using Equation (1.1).

$$ZT = \frac{\sigma S^2 T}{\kappa} \qquad (1.1)$$

From this equation, it is clear that thermoelectric optimization involves reducing thermal conductivity and increasing both the electrical conductivity and the Seebeck coefficient. There are two components which sum to the total thermal conductivity, electron and lattice contributions. The electron contribution to thermal conductivity is proportional to electrical conductivity according to the Wiedemann-Franz law, which makes optimization of thermoelectrics difficult [7]. A desirable material acts as a "phonon-glass electronic-crystal" which would scatter phonons, reducing the lattice contribution to thermal conductivity, yet allow electrons to move easily though the

material. This sums up some of the difficulties of designing efficient thermoelectrics; optimizing one property typically involves altering the other properties of the material in a negative way.

Advancements in thermoelectric materials have increased rapidly in recent years with the emergence of the field of nanoscience. Much of the research that has gone into modern thermoelectric materials began with theoretical calculations on quantum well superlattice structures of Bi_2Te_s [8]. This initial research showed that if layers of bismuth telluride could be made into layers 1 nm in thickness, the ZT of Bi_2Te_3 superlattice structures could be near 13. This is possible since electrons would be restricted to moving only in two dimensions, with the additional benefit of scattering phonons as they move between layers. This enhancement also is dependent upon the anisotropic material properties in Bi_2Te_3. This work was also expanded to include 1d nanowires as a possible method of increasing the ZT of Bi_2Te_3 by the same factor [9]. This new work suggested this is possible when the width of the nanowire was smaller than the de Broglie wavelength of the material, about 5 Å in Bi_2Te_3. This was later experimentally confirmed as a valid approach by measuring $PbTe/Pb_{1-x}Ee_xTe$ superlattice systems [10].

Although these studies showed a vast potential for ZT enhancement, the methods used to create the materials were often costly. Superlattice and nanowire structures require expensive fabrication methods that are not easy to create on a large scale for manufacturing when compared to traditional bulk crystal growth techniques. An alternative concept to reducing the lattice conductivity of the material is random nanostructures. Phonons, carriers of heat, are able to travel relatively quickly through a

single crystal of a material, but are scattered when moving from one crystal to another.

If the average crystal size of the material is decreased, then the density of interfaces

between crystals increases. If the crystals can be reduced to nanoscale lengths, then the

number of interfaces could be high enough to impede phonons from moving freely. This

was proven by creating nanoparticles via high energy ball milling [3]. In that study, the

ZT was improved at all temperatures over a range from 25°C to 250°C as seen in figure

1.2. The particles in the planetary ball mill were reduced to an average size of 20nm,

with some particles as large as 50nm and as small as 5 nm.
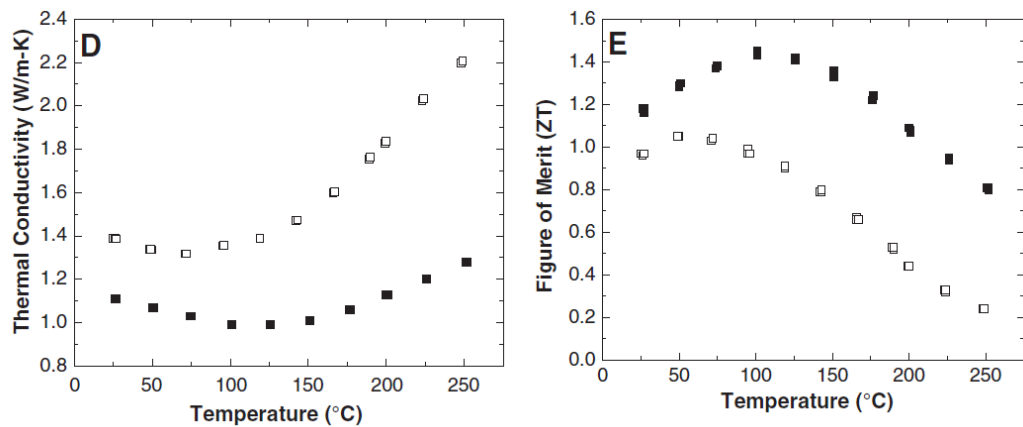
Figure 1.2. Thermal conductivity (left) and the dimensionless figure of merit (right) of planetary ball milled $Bi_{0.5}Sb_{1.5}Te_3$ [3].

There has been a lot of research on planetary ball milling of thermoelectric

materials since these initial findings. Much of this research has focused on analyzing or

improving upon a specific aspect of thermoelectrics. The morphology of the crystals was

analyzed after subjecting the raw materials to different planetary milling conditions [11].

This study also found that nanocrystalline Bi_2Te_3 was able to form after only 5 hours of milling in a planetary mill.

There are also papers that discuss making a solid pellet from the milled powders. There are two main types of pellet formation reported in literature, spark plasma sintering (SPS) and hot pressing. SPS is a process in which the powders are compressed at high pressures then subjected to pulses of DC current which consolidate the powders into a solid pellet [12]. Although this process creates high temperatures within the sample, it is for short periods of time so grain growth in the sample is limited. It should be noted that there is some research suggesting plasma is not created nor is there any sparking during the SPS process, although its efficacy as a powder compaction technique is not challenged [13].

Alternatively, hot pressing is a method in which the powders are once again pressed into a pellet, but an external heat source is applied to the powders. The heat source is typically a lower temperature than those in spark plasma sintering, however the sample is subjected to heat for a longer period of time. There have been studies into the effects of each of these types of powder compaction, including the effects on thermoelectric properties. Figure of merit was shown to increase with hot pressing time and temperature up about 340°C and 4h; however, no report on grain sizes before and after this process was reported [14].

1.4   Ball Milling Techniques

Ball milling is a well understood process in which material that is used to grind material into smaller particles. This is done by adding grinding media, which are typically hard round pieces of metal or ceramic, into a vessel also containing the material to be ground. The vessel is then moved about in various ways, depending on the type of mill, in order to cause collisions between grinding media and thus crush the material into smaller pieces.

There are two broad categories of ball mills, low-energy and high-energy. The difference between these two types of mills is the amount of energy applied to the material to be ground and the energy input to the milling machine. Low energy ball mills, such as tumble ball mills and vibrating mills, have been used in many powder production industries such as paints and inks [15] and cement production [16]. A tumble ball mill, one of the most common types of mills, operates simply by rotating the jar filled with media and material. The action of the balls within the vessel is dependent upon the speed of rotation, with three possible regimes. At low rotational speeds, the balls do not climb very high along the side of the jar and the balls simply tumble over each other during rotation; a process known as cascading. As the rotational speed is increased, the balls are able elevate high on the side of the jar and fall without impacting other balls; a process known as cataracting. Finally, when the rotational speed is increased even higher, the balls are stuck to the outer edge of the jar as the centrifugal forces take over. The speed at which centrifugal forces dominate is known as the critical speed of the jar,

and is a function of the diameter of the grinding media and the inner diameter of the jar they are rotating in [17]. These processes are depicted in figure 1.3.
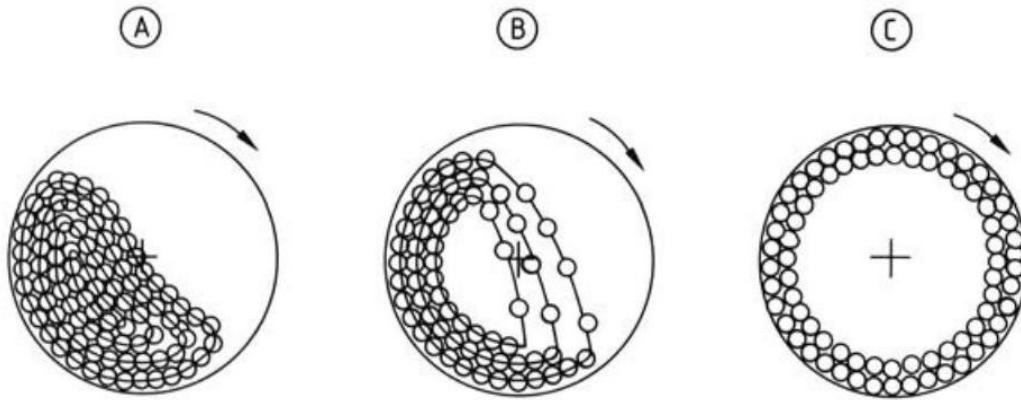
Figure 1.3. Three regimes during ball milling showing cascading (A), cataracting (B), and centrifugal (C). Figure was taken from reference [18].

High-energy ball mills have been of much interest in the scientific community and have become a reliable method of manufacturing nanoparticles. It has also been used for mechanical alloying, which describes combining powders of individual elements and milling until the material is one continuous alloy. The most commonly utilized ball mill related to the production of thermoelectric nano-materials has been the planetary mill [3,14,19-24]. This mill is more time efficient due to its ability to rotate about two axes, creating strong centrifugal forces that throw the grinding media onto the side of the jar with a high amount of force. This process is depicted in figure 1.4.

Horizontal section

Movement of the
supporting disc

Centrifugal
force

Rotation of the milling bowl
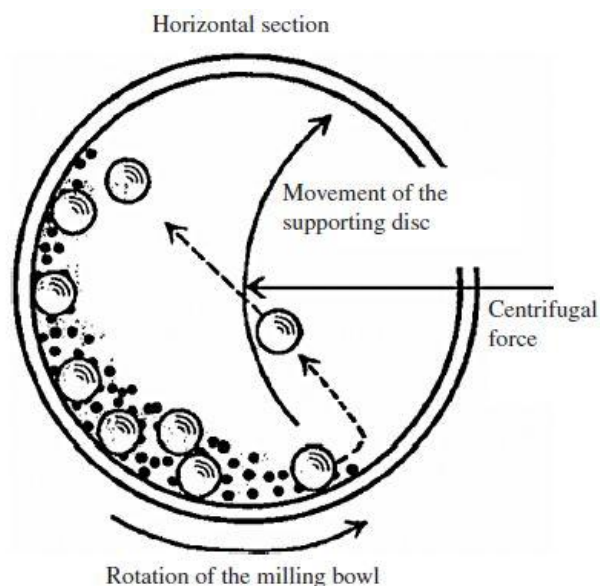
Figure 1.4. Schematic showing the dynamics of a planetary ball mill
(http://www.understandingnano.com/nanomaterial-synthesis-ball-milling.html).

Using these higher forces in order to grind the materials quicker comes at a price.

Planetary mills can't be as large as tumble ball mills due to the high forces achieved

during the milling process. Also, the motion of media inside of planetary mills is hard to

observe making verification of simulations difficult [25]. These factors limit the use of

planetary mills outside of a laboratory setting. Alternatively, the scale-up of tumble ball

mills has been studied much more extensively. Tumble ball mills, as stated earlier, have

been used much more in industrial settings such as cement production, paints and inks,

etc. This development also has been aided by the relative ease and understanding of

ball movement inside the mill. It has been shown that using the discrete element

method, modeling collisions as spring-dashpots, matches experimental results closely

[26]. Two commercially available large scale ball mills, one planetary and one tumble,

are shown in figure 1.4 in order to demonstrate the difference in size between the two

types. The tumble ball mill has a capacity of 15300 liters, while the planetary mill only

has a capacity of 1 L.

Figure 1.5. An industrial sized tumble ball mill from Shanghai Minggong is shown on the left (http://www.mg-ballmill.com/grinding-mills/Ball-Mill-Supplier.htm) compared to a Retsch PM 400 planetary mill (right).

CHAPTER 2.   MATERIAL SYNTHESIS

2.1   Sample Preparation

The first step in creating nanoscale thermoelectrics via ball milling is to choose the bulk starting materials. The selection of starting materials is dependent upon whether the material is desired to be n-type or p-type, both of which are needed to create a device. The semiconductor doping type is dependent upon whether the dopant atoms donate holes (p-type) or electrons (n-type) as charge carriers. For this study, antimony (Sb) was used to create the p-type materials, where Sb atoms diffuse into the lattice and replace Bi atoms. Selenium (Se) was used to create n-type materials, where the Se atoms diffuse into the lattice and replace Te atoms.

To start the ball milling process, the elements are added to a 16 oz. dented jar in stoichiometric ratios depending on the final composition desired. For this study, p-type $Bi_{0.5}Sb_{1.5}Te_3$ (BST) and n-type $Bi_2Te_{2.7}Se_{0.3}$ (BTS) were desired as the final compositions. After adding the materials, the grinding media must be added at a 2:1 ratio of 3/8" to 3/16" diameter media. 100 mL of ethanol was added to the jar in order reduce the rate of oxidation in two ways: keeping the temperature of the materials low and not allowing the material to come into contact with oxygen in the air. Before closing the jar, it was

purged with nitrogen as a further measure of preventing oxidation. After closing the lid of the jar, it was sealed with putty-like poster tack and duct tape to prevent air from getting into the jar.

Once the jar was prepared it was placed on the milling machine, which is just two rubber rollers that spin the jar horizontally. The jar was milled for two to five days, then the contents were emptied and the ethanol/material solution was separated from the grinding media. The solution was dried in an oven at 70°C in order to evaporate the ethanol from the materials. After drying, the material was sieved in a 106μm sieve in order to separate any large chunks from the smaller sized particles.

At this point, the powders were ready to be formed into a pellet. To do this, a hot press was used. This piece of equipment consists of two hot plates which are able to apply pressure to a die. The die used to for the pellets was a stainless steel cylinder with a diameter of 15 mm. Pellets were formed under a pressure of 210 MPa and temperature of 420K. Figure 2.1 shows the equipment used during the entire process.
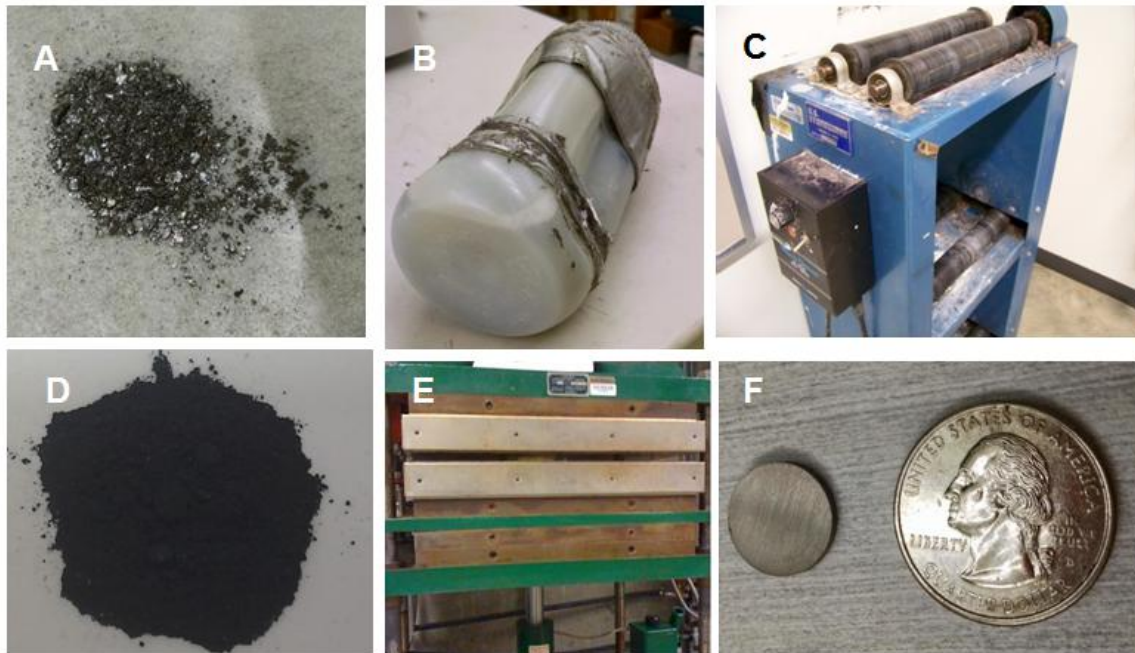
Figure 2.1. milling process showing starting materials (A), dented milling jar (B), ball mill machine (C), milled powder (D), hot press (E), and the final pellet shown next to an American quarter (F).

2.2   Ball Milling Parameters

In order to optimize the ball milling process, the size of particles must be analyzed. The Scherrer equation [27] was used to determine the resulting particle size, using Equation (2.1) with values obtained from XRD analysis. Results from the size analysis using XRD were then confirmed visually using both TEM and SEM.

$$L = \frac{k\lambda}{\beta cos\theta} \qquad\qquad (2.1)$$

Different grinding vessels and media were tested to find the optimal grinding rates, contamination rates, and final grain size. Trials with both 32 oz. and 16oz. jars

with and without indentations were attempted, where all vessels were made from high-density polyethylene. Grinding media was also varied from 3/16" to 1/2" in diameter in two different material types: tungsten carbide and zirconia.

During initial testing, the weight yield of powder from the ball milling process was twice as heavy as the sum of the starting materials put into the jar indicating severe contamination. XRD analysis of the samples milled with tungsten carbide revealed peaks located at angles associated with tungsten carbide. This means the source of contamination during the milling came from the grinding media. This was unable to be confirmed using XRD in the cases using zirconia due to its amorphous nature. Although zirconia contamination can't be observed in XRD, color indicates it is still most likely coming from zirconia.
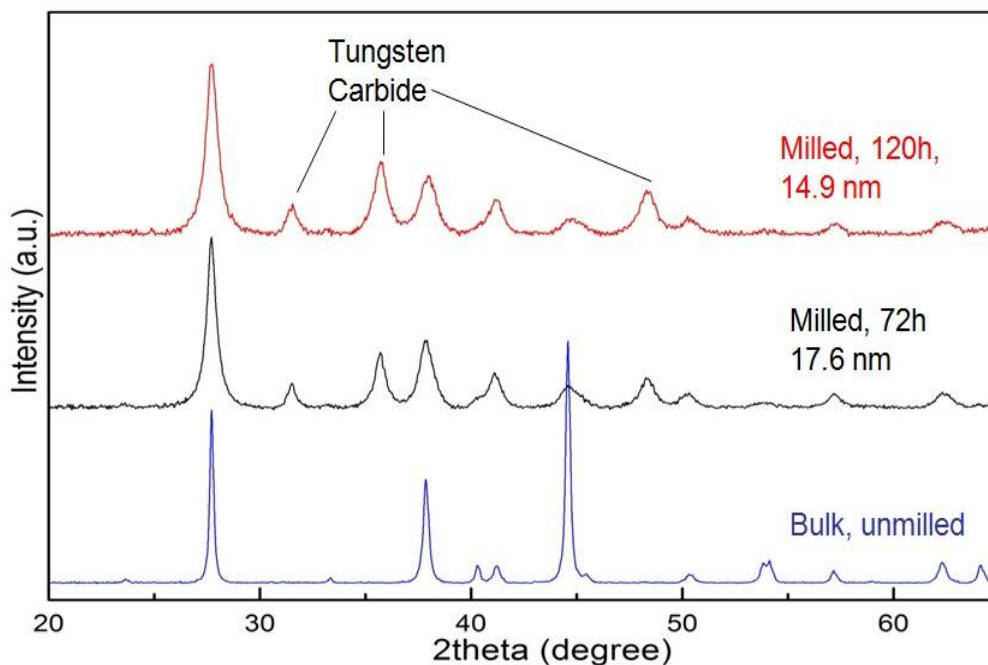

Figure 2.2. XRD results of milled Bi2Te3 with tungsten carbide. Extra peaks in the milled product correspond to tungsten carbide contamination.

By weight, contamination in the tungsten carbide media was less severe than the zirconia yet still reduces particle size more efficiently. This can be explained by analyzing the properties of each material, specifically hardness and the compressive strength. Relevant material properties are shown in table 2.1, showing that tungsten carbide has a higher compressive strength and hardness. A harder material will deform less upon impact than soft materials. In ball milling, the material is broken up as the ball falls from the top of the jar to the bottom and impacts other balls, trapping material in between them. The force that gets applied to the materials to grind is related to the surface area of the collision. A large surface area will distribute the load more evenly, resulting in a smaller force on each individual particle. This means soft grinding media can deform upon impact and actually decrease the effectiveness of the grinding. The compressive strength of the material measures the ability to resist fracture upon compression, which is related to contamination rates. Tungsten Carbide exhibits a lower compressive strength, which makes the material more resistant to fracturing on impact and reduces contamination.

Table 2.1. Relevant material properties of both zirconia and tungsten carbide. Compressive strength of zirconia was measured by ferrocermic using ASTM standard C773, while tungsten carbide was measured with 3% cobalt added from NIST Structural Dynamics Database.

Material	Hardness (Knoop scale)	Compressive strength
Zirconia	1200 [28]	12.5 MPa[29]
Tungsten Carbide	1880 [28]	3.1-5.9 GPa [30]

After determining that tungsten carbide was a more effective grinding media, the contamination still was an issue. One method of reducing the contamination was to alter the weight ratio of grinding media to the material. To investigate different grinding ratios, the amount of material added to the jar was varied. The amount of grinding media had to remain the same, since altering the amount of media in the jars affects how the balls move inside the jar. Three different amounts of material were tested: 10g, 20g, and 30g. After milling, XRD was used to determine the composition of the milled materials. Results from the XRD analysis can be seen in figure 2.3.
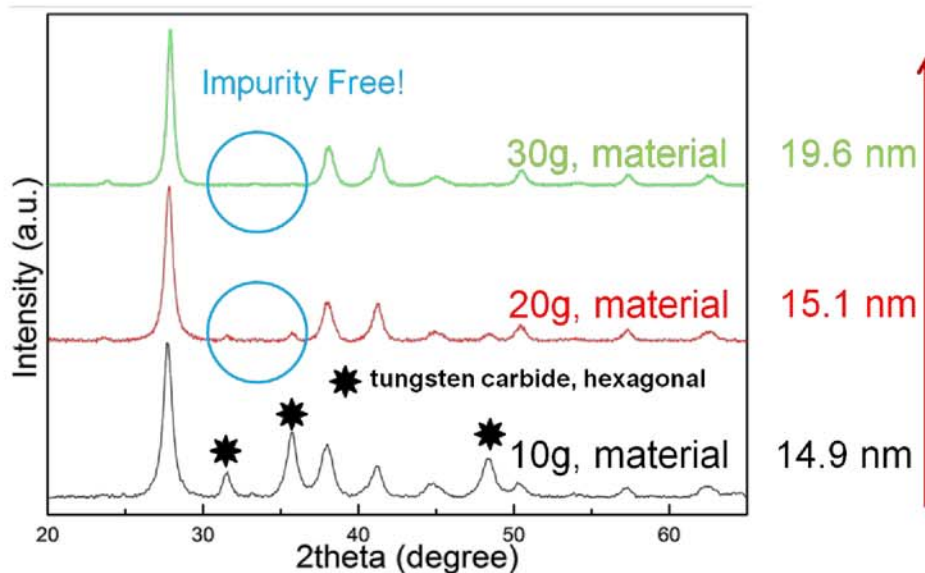

Figure 2.3. XRD results showing the decrease in contamination as the amount of material is increased.

From these results, it is clear that a reduction in contamination can be achieved by paying close attention to the ratio of material to grinding ratio. As the amount of material was increased, the tungsten carbide present in the sample

decreased significantly. Just as important is the lack of decrease in grinding

efficiency, which means large amounts of material can be processed at once. When

the amount of material was tripled, the final particle size changes by less than 5nm

which is very encouraging. From this data, the weight ratio of tungsten carbide

media to material should remain less than 45:1.

2.3   Doping and Ball Milling

For previous studies on the efficacy of ball milling, Bi_2Te_3 was used. For

practical applications, this needs to be doped to create both n-type and p-type

semiconductors. To do this, other elements are added to bismuth telluride before

the milling process begins. The idea behind adding the elements is that mechanical

alloying will occur, where the dopant atoms diffuse into the lattice and the resulting

material is one phase. This process of diffusion requires energy in order to force

atoms into the lattice. This process has been shown to work with other materials,

such as nano-SiC in Bi_2Te_3, but using a planetary ball mill [20,21]. This is an

important distinction since planetary mills are higher energy than tumble mills,

providing more energy for dopant atoms to diffuse into the lattice.

As stated previously, Sb was added to create p-type $Bi_{0.5}Sb_{1.5}Te_3$ while Se was

added to create n-type $Bi_2Te_{2.7}Se_{0.3}$. After milling, the composition of the materials

were analyzed with XRD and compared to the JCPDS database. It was found that

enough energy was provided to the n-type material in order for it to become one

continuous phase of $Bi_2Te_{2.7}Se_{0.3}$. However; this was not the case for the p-type

material. XRD showed that it had formed a mixture of two compounds, Bi_2Te_3 and

Sb_2Te_3. The reason for this discrepancy lies in the energy required to diffuse the

dopant atoms into the lattice. An atom in a lattice exists at the lowest point of the

parabolic potential energy curve [31]. If another atom is to diffuse into the lattice, it

must have more energy than the edge of the parabolic potential. Te atoms have

weak bonds in Bi_2Te_3 so less energy is required for Se atoms to diffuse into the

lattice. This is not the case for Bi atoms, which have stronger bonds and require

more energy than is provided via ball milling alone.

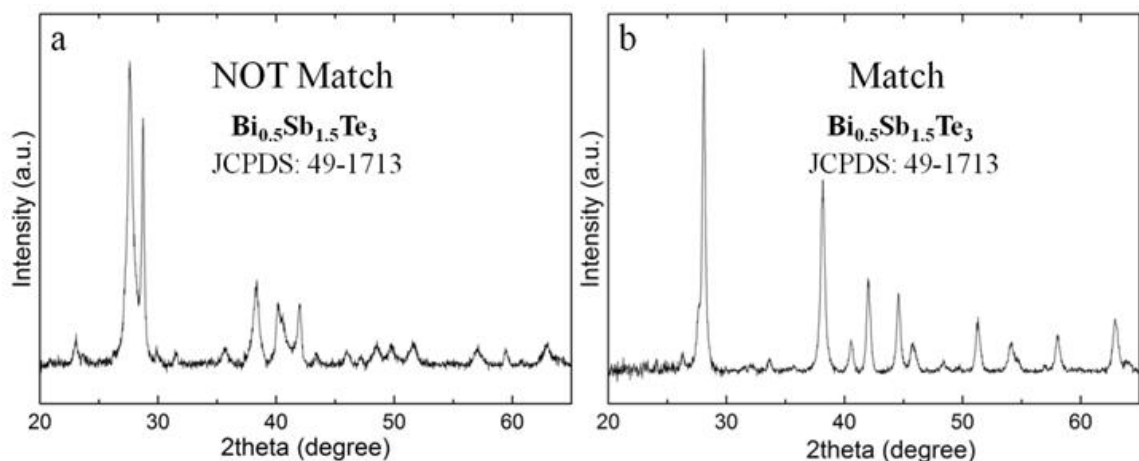Figure 2.4. XRD results showing the material before annealing (a) and after
annealing (b).

One approach to provide enough energy for diffusion is to thermally anneal

the sample. This is a step performed in an inert atmosphere, to prevent oxidation, in

which the sample is heated to 300F. XRD confirmed that thermal annealing provided

enough energy to diffuse dopant atoms into the lattice, as seen in fig. 2.4. In fig. 2.4a

there are two distinct peaks located near 28°, which consolidates into a single peak

after annealing. This indicates, according to the JCPDS database, that the material is

of one phase. Annealing does, however, affect the thermoelectric properties of the

material, which will be discussed at further detail in chapter 4.

2.4   Milling Time

A key factor in the ball milling process is the effect of milling time on results

such as final grain size and contamination rates. Three influences are at play when

determining the correct milling time: contamination rate, grinding efficiency, and

particle size. Previous work using planetary mills shows that the grinding efficiency

decreases to almost zero during long milling. That is, the particle size of Bi_2Te_3 will

essentially plateau after a certain amount of time [20]. One of the reasons this is

common in Bi_2Te_3 is the adiabatic heating that results from ball collisions. An

important result from that study shows that lower energy collisions result in smaller

particles, which seems contradictory to what one might expect. These conclusions

came from a study on planetary mills; however, the principles remain the same.

There should exist a point at which the rate of size reduction is no longer beneficial

enough to overcome the decrease in performance arising from contamination.
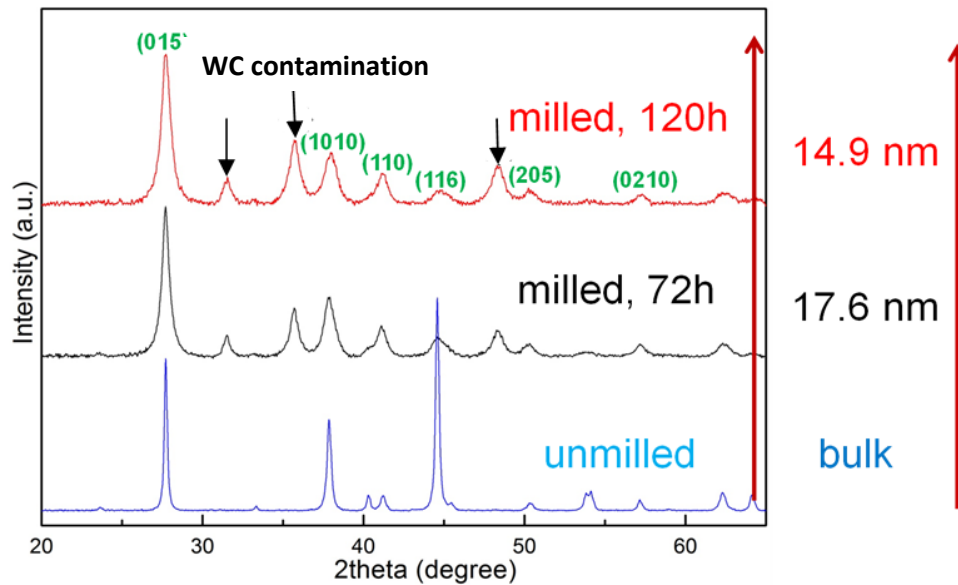
Figure 2.5. XRD analysis of Bi_2Te_3 for various milling times of 0h, 72h, and 120h, along with corresponding average particle size.

Figure 2.5 shows XRD analysis with corresponding particle sizes for milling times of 0 hours, 72 hours, and 120 hours. It should be noted that this study was completed before the correct ratio of grinding media to material was found, so contamination exists in all samples. When comparing the 72 hour and 120 hour samples, very little size reduction takes place. However; the relative height of the tungsten carbide peaks shows that contamination increased in the extra 48 hours of milling time.

2.5   Hot Pressing Setups

For most of the hot pressing, the setup shown in fig. 2.1e was utilized. This setup consists of two heating plates compressing the punches which are heated from the ends, with convective losses meaning the temperature of the powders was not 300°F, but rather the plates were. The other disadvantage to this setup was that it was not performed in an inert atmosphere, which could mean oxidation is occurring. At room temperature, it has been reported that a 1.5nm layer of oxide can form in the first two weeks, with the rate of oxidation slowing significantly after that to the point where after 250 days the layer will only be about 2.2nm thick [32]. A significant increase in oxidation has been shown to occur around 400°C using thermogravimetric analysis, although no oxidation rates were reported [32].

Although the temperatures reported as having a significant increase in oxidation occur at 400°C, elevated oxidation rates are to some degree expected to rise along with temperature. For that reason, the method of hot pressing in an inert atmosphere was investigated. To do this, an existing cold press setup in a glove box, with O_2 levels of less than 0.1 ppm, was modified. A flexible heater was wrapped around the die used during hot pressing and its temperature was controlled using a Sestos d1s-vr-220 PID temperature controller. A visual of the setup used is shown in figure 2.6.

Figure 2.6. Hot press setup in an inert atmosphere (Ar).

It should be noted that there is an expected difference in temperature between the two hot press setups, although each was set to 300°F. The 300°F pressing temperature is actually the temperature of the plates, which are on the top and bottom of the punches for the die. This means the temperature of the powders will be lower than the 300°F of the plates due to losses between the top of the press and the bottom. In the inert hot pressing setup the heater is around the die, which is much closer to the locations of the powders. Although a higher powder temperature is most likely achieved with the inert hot pressing setup, there was not enough thermal energy provided to the powders to replace the annealing process. XRD results still showed two distinct peaks located at 28°, indicating two separate phases of Bi_2Te_3 and Sb_2Te_3 were present. It is possible that increasing the hot pressing temperature beyond 300°F could reduce the need for annealing, although this was not investigated.

CHAPTER 3.   MORPHOLOGY

3.1   SEM and TEM Imaging

SEM and TEM images were taken in order to confirm the particle size

calculated using XRD analysis as well as visually inspect the particles.
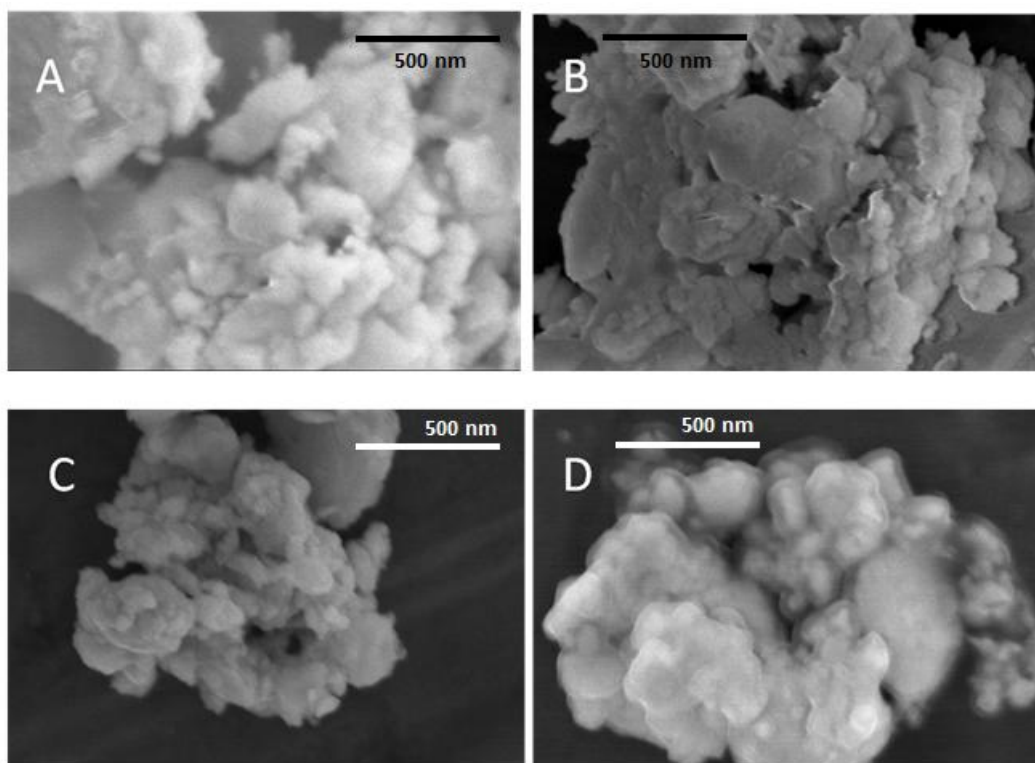
Figure 3.1. SEM images of particles after milling for 24h (A), 48h (B), 120h (C), 168h (D).
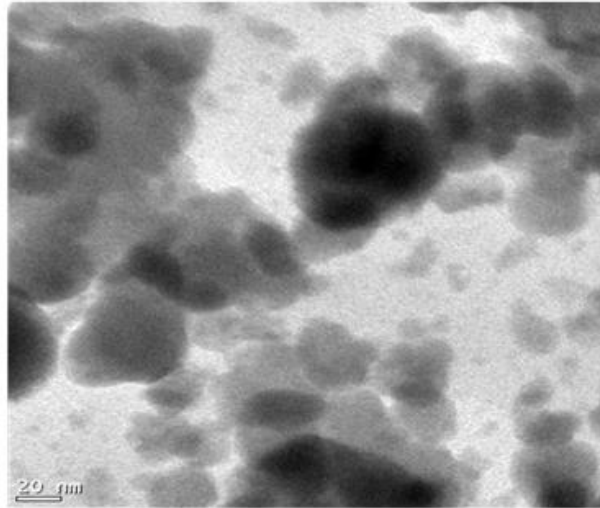
Figure 3.2. TEM image of Bi_2Te_3 milled for 120 hours.

The SEM images appear to show large crystals that are much larger than the average size calculated using XRD data. TEM shows much smaller crystals in this mix, with some particles being as small as 5 nm, which agrees well with XRD data. There are two possible reasons for the discrepancy between SEM imaging and the XRD data. First, the resolution of the SEM is limited, and is not able to capture the smallest particles as well as the TEM is able to. Second, individual particles may have clumped together, making the particles visible by SEM actually made up of many crystals.

3.2 Crystal Dimensionality

The dimensionality of the thermoelectric crystals is very important to the efficiency of the material. Early pioneering research in this field suggested that creating superlattice quantum well structures with a thickness of about 1 nm could, in theory, increase the ZT of the material by 13 times [8,9]. While an advancement in

ZT like this has not been recognized experimentally, it has inspired a great amount of

research into nanostructured thermoelectrics. One goal has been to create and

isolate individual stacks of Bi_2Te_3, known as quintuples due to the 5 layer stacks of

atoms in one crystal which are Te-Bi-Te-Bi-Te. This has been done successfully,

utilizing mechanical cleavage in order to separate the quintuples from each other

[33]. One reason this was possible is because the quintuples are separated by Van

der Waals bonds which are weaker than the bonding in the quintuples [34]. Upon

thermoelectric characterization, a reported increase in ZT of 30-40% can be made by

stacking these crystals to create a superlattice.

One characteristic of these low-dimensional structures is a shift in the raman

spectra of the materials. As the layers of bismuth telluride become very thin, new

peaks emerge due to the high level of asymmetry due to looking at individual atoms

as opposed to thicker layers with many atoms [33]. One peak that becomes Raman

active in few quintuple layers is the A_{1u} peak located near 120 cm^{-1}. Raman

spectroscopy was used to measure the Raman spectra of Bi_2Te_3 nanoparticles

created via ball-milling, with the spectra shown in fig. 3.2. The A_{1u} peak in a sample

milled for 4 days, resulting in an average crystal size of 15.1 nm, shows that these 2D

structures have been created in our samples.
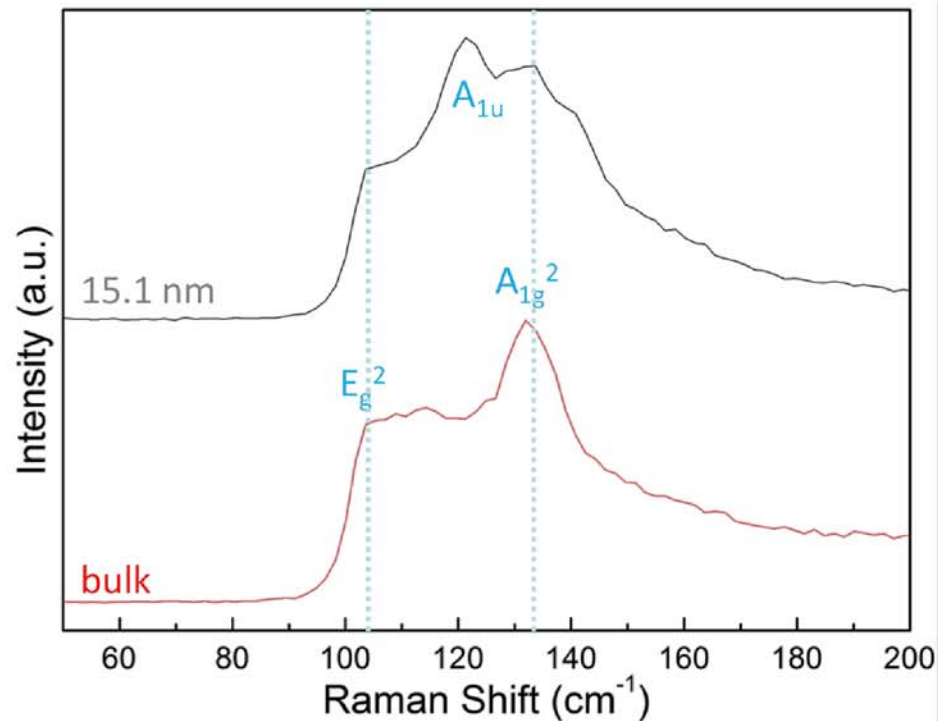
Figure 3.3. Raman spectra of both bulk and ball-milled Bi$_2$Te$_3$.

One possible reason these 2D structures are formed is due to the movement of media inside the milling jar. As media is falling from the top to the bottom of the jar during rotation, the ball is actually impacting other balls on the way down. The media tumbles down the hill of grinding media that is present during the grinding process. It is possible that not only do collisions reduce particle size upon impact, but as the ball slides down the hill it creates a shearing force for material trapped between the falling media and the media on the hill portion of the jar. This shearing could break bonds between quintuples that are not able to sustain a large shearing load.

It is important to discuss that although the 2D particles are created, their thermoelectric properties are not able to be fully utilized. First, the 2D crystals were

unable to be separated from the crystals with other dimensionsalities. This process

is critical since 2D crystals would need to be stacked in order to enhance

thermoelectric performance. In addition, controlling the thickness of the layers is

critical to good thermoelectric performance [8-10].

CHAPTER 4.   THERMOELECTRIC CHARACTERIZATON

The efficiency of thermoelectric materials is characterized by the figure of merit, which is dependent upon electrical conductivity, Seebeck coefficient and the thermal conductivity of the material. In order to measure the efficiency, each of these properties must be evaluated. A 4-probe Kiethley 4200 Semiconductor Parameter Analyzer was used to measure electrical conductivity and an MMR SB-100 Programmable Seebeck controller and MMR K-20 Programmable Temperature Controller was used to measure the Seebeck coefficient.

4.1   Seebeck Coefficient

The Seebeck coefficient is the measure of a voltage difference resulting from a temperature difference across the thermoelectric material. This is not to be confused with the Peltier effect, which is the creation of hot and cold zones due to current flowing through a conductor. The Seebeck coefficient is inversely related to the carrier concentration, n, through Equation (4.1) [22].

$$S = \frac{8\pi^2 k_b^2 T}{3Ch^2} m^* \left(\frac{\pi}{3n}\right)^{2/3} \tag{4.1}$$

Previous work with high-energy ball milling, specifically planetary, has shown that carrier concentration is sensitive to the time of ball milling, which affects both the Seebeck coefficient and electrical conductivity. In both n-type and p-type materials, antisite defects in which Bi atoms replace Te atoms contribute to an increase in carrier concentration at long ball milling times of one day or more [22,23]. This has differing effects on the two materials though. When Bi replaces Te in the lattice, it acts as p-type doping since the defect consumes 2 electrons and produces 4 holes [22,23]. This means the carrier concentration is increased in p-type materials while it is decreased in n-type materials. It is unclear whether this is able to take place with the lower energies provided by tumble ball milling, and more research on the effect of tumble ball milling on carrier concentration would be needed.

Seebeck coefficients for samples doped with antimony and selenium are shown in figure 4.1. These results include the Seebeck coefficient for each material before and after being annealed at 400°C. In both cases, the Seebeck coefficient was improved after annealing.
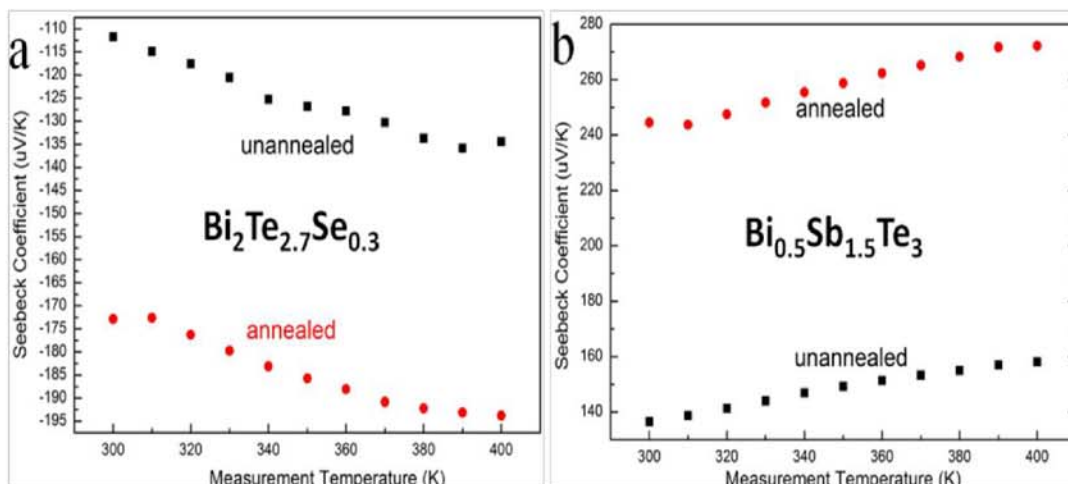
Figure 4.1. Seebeck coefficients of (a) n-type $Bi_2Te_{2.7}Se_{0.3}$ and (b) p-type $Bi_{0.5}Sb_{1.5}Te_3$, where annealing was performed at 400°C.

4.2 Thermal Conductivity

Thermal measurements were performed by the Thermophysical Properties Research Laboratory (TPRC), Inc. in West Lafayette, IN then confirmed using both an IR camera setup and 3-omega methods. When sent to the TPRC, thermal measurements were made by using both the specific heat and thermal diffusivity of the samples. Specific heat was measured with a Perkin-Elmer Model DSC-4 Differential Scanning Calorimeter and thermal diffusivity was measured using the laser flash technique. Thermal conductivity is calculated as the product of the thermal diffusivity, specific heat, and sample density.

Thermal measurements performed using the laser flash technique are shown in figure 4.2. These measurements exhibit an unexpected drop in thermal conductivity at 100°C, which appears to be an outlier in the data. Looking further

into the data, specific heat and thermal diffusivity also exhibit apparent outliers at this temperature.
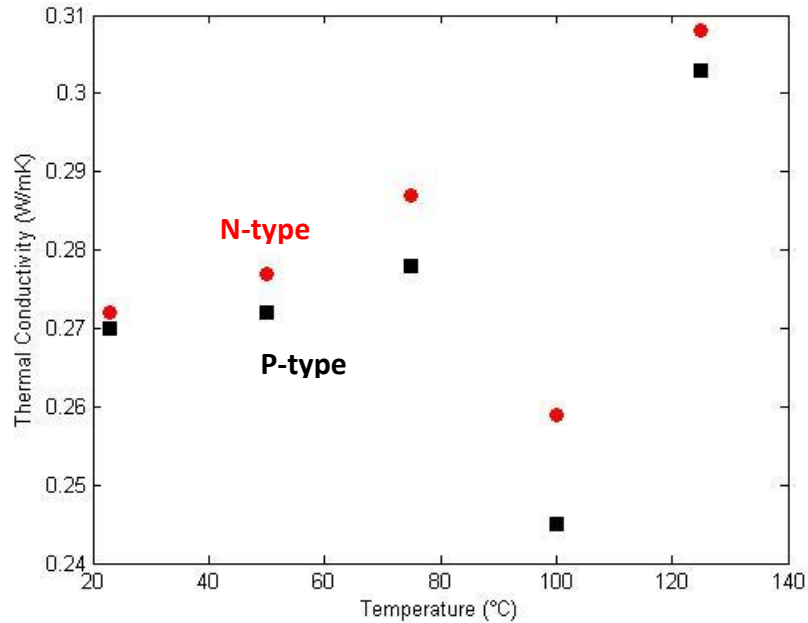
Figure 4.2. Thermal conductivity of both n-type and p-type materials measured using the laser flash technique.

To confirm the results from the laser flash technique, thermal conductivity was also measured using an IR camera setup. In this setup, a sample is placed between two heaters, sandwiched between two reference materials with known thermal conductivity. The stack of reference-sample-reference is then placed between two heaters to elevate the temperature of the entire stack to about 45°C. Once the entire stack is at one temperature, the IR camera is calibrated to find the emissivity at each point of the stack. Following this calibration, one side of the stack is cooled by flowing water through the heating plate in order to create a temperature difference across the stack. After reaching steady state, the camera

takes a temperature map of the stack. This is performed with varying temperature

differentials over the stack and these maps are used to calculate the thermal

conductivity.

To get the thermal conductivity of the sample, the heat flux flowing through

the sample needs to be calculated. This is the purpose of using the reference layers,

as the heat flux through each reference layer can be calculated using Fourier's law.

The slope of temperature is found from the temperature map, the thermal

conductivity of the reference is already known, and the area is not important since

the area of sample and references are all the same. Once the heat flux is known,

then Fourier's law is solved for the thermal conductivity of the sample. An example

of the temperature map obtained from the IR camera is shown in figure 4.3, along

with the temperature profile of a typical case.
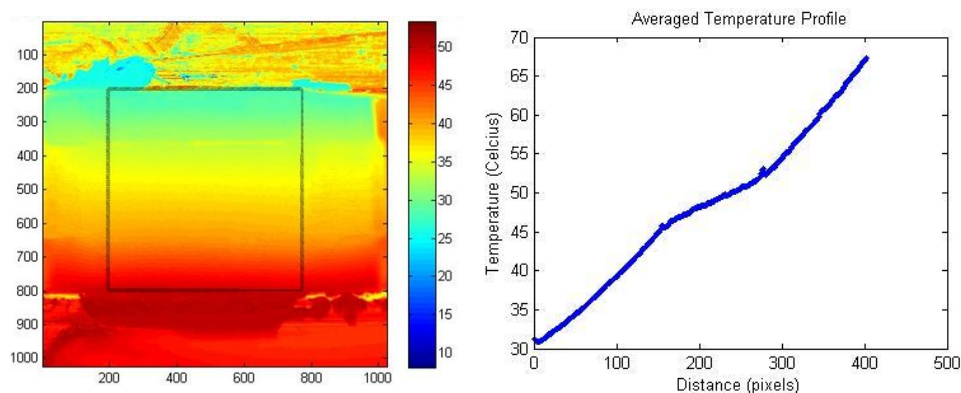

Figure 4.3. A temperature map from the IR camera with the sample shown in a box
(left) and the average profile of the boxed regions (right).

The drawback to using the IR camera setup in order to test thermal

conductivity is that it does not eliminate convective and radiative losses when

measuring the sample. This could be eliminated if the sample is placed in a vacuum

chamber, but this was not able to be explored for this project. Evidence of losses can be found within the temperature profiles in the temperature profiles obtained from the IR camera. Since heat transfer due to radiation and convection increases with the sample, the slopes of the temperature profiles will change with the temperature of the stack. It is expected that the slope of temperature will be steeper in hotter regions of the sample, due to the increased heat transfer. This is confirmed in the temperature profile of the stack, where most samples show a 20-30% difference in the slopes of the reference layers.

A MATLAB code was written that uses the temperature map as well as some other user inputs to approximate the loss at each temperature point. This is a numeric approximation that considers each temperature point as a small cylinder and evaluates losses at each small cylinder. The heat loss is then summed for each point in order to quantify the total losses.

In order to approximate convection, the Churchill-Chu relation for natural convection around a cylinder was adopted, which is shown in Equation (4.2) [35].

$$Nu = 0.36 + 0.518 \left(\frac{Ra}{\left[1 + \left(0.559/Pr \right)^{9/16} \right]^{16/9}} \right)^{1/4} \qquad (4.2)$$

This relation is valid for $10^{-6} < Ra < 10^{9}$ and all Pr, which is valid since each of these conditions are met by all reasonable experimental conditions. Values for Ra and Pr and calculated based on the fluid properties at room temperature. Once the Nusselt number is known, the convection coefficient h can be found using the definition of

the Nusselt number. As shown in Equation (4.3), the heat transfer coefficient is then

calculated using Newton's law of cooling.

$$h = \frac{Nu*k_{air}}{L} \tag{4.3}$$

Radiation losses were then calculated using Equation (4.4), which shows the

radiation exchange between an object and its surroundings.

$$q_{rad} = \varepsilon\sigma A(T_{sample}{}^4 - T_{surr}{}^4) \tag{4.4}$$

Finally, the conductive heat transfer was calculated using the thermal conductivity

values obtained using the IR camera and the temperature difference across the

entire sample. The thermal resistance of each layer of the stack was summed to find

a constant value for conduction through the sample. Although this may seem

counter intuitive to use the value found using the IR camera to evaluate the error in

the process, it can still give a good picture of the losses that occur in the setup.

Results from analyzing the errors show that only 70-80% of the total heat

transfer taking place in the stack is due to conduction, with the rest split evenly

between radiation and convection. Fig. 4.4 shows the heat transfer via each of the

nodes for the entire length of the sample. It is important to remember that this

represents the test case at which the sample is the hottest.
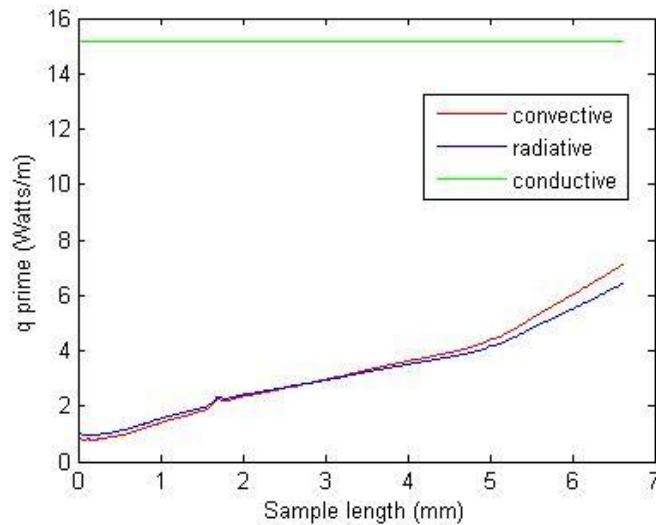
Figure 4.4. Heat transfer via all three modes along the sample during the hottest test case of Bi_2Te_3 with no graphene added.

Of the methods used to measure thermal conductivity, they have all showed a significantly lower value than those reported by other groups. Pellets created from bulk Bi_2Te_3 have thermal conductivities reported as 1.4 W/mK and planetary milled samples have thermal conductivities of 1.1 W/mK, with both values taken at room temperature [3].

4.3   Graphene Additives

The main limitation of these materials is the electrical conductivity, as seen in table 4.1, which is significantly lower than those reported by others in literature. One method of increasing this electrical conductivity is to add small amounts of graphene, which is known to have a very high electrical conductivity. Graphene additives have not been studied extensively, only when adding to n-type materials. In this study, the electrical conductivity was actually shown to decrease the

conductivity [36], although this is most likely due to the p-type doping effects of graphene.

One consideration of using graphene is that in addition to having a high electrical conductivity, it also shows high thermal conductivity. Using this IR camera setup, samples of p-type $Bi_{0.5}Sb_{1.5}Te_3$ with 0%, 0.01% and 0.05% graphene by weight were measured. Due to the presence of losses outlined in the previous section, the sample thermal conductivity was calculated using both reference layers, as well as each of the individual layers on the left and right sides. Since the conductive heat flux in the sample is expected to be higher than the cold side and lower than the warm side, this gives an upper and lower bound to the thermal conductivity.

Table 4.1. Summary of thermal results of samples containing graphene at 0%, 0.01% and 0.05% by weight. The error is also shown as the difference between the slopes on the left and rights sides compared with the prediction of convective and radiative losses predicted by the program. *testing with 0.05% graphene additives is not believed to be accurate.

	Thermal conductivity in $Wm^{-1}K^{-1}$			Error	
Sample type	Using cold reference	Using hot reference	Using both references	Average difference between slopes	Numerical Prediction
BST + no graphene	0.320	0.430	0.359	27.0%	33.28%
BST + 0.01% graphene	0.416	0.525	0.466	18.3%	19.96%
BST + 0.05% graphene	0.201*	0.212*	0.211*	4.3%	18.7%

From the results in table 4.1, it is apparent that graphene does have an impact on the thermal conductivity, although with mixed results. Adding 0.01% graphene adds to the thermal conductivity as expected, but the same case is not seen in the case with 0.05% graphene. The reason for this is due to errors in testing,

and it is believed the 0.05% graphene results are incorrect. The measurement was

performed using a sample significantly thinner than the samples in other

measurements. The temperature profile showed a much less consistent slope and

exhibited significantly more variation than other samples.

Data for electrical conductivity and the Seebeck coefficient is still being

gathered for samples containing graphene and will be included when available.

4.4   Figure of Merit

Samples created via tumble ball milling in this study exhibit much different

properties than both bulk Bi_2Te_3 and samples created via high-energy ball milling.

Table 4.2 summarizes key results and compares the measured properties against

some other state of the art nanostructured materials. From these results, it is clear

that tumble ball milled samples exhibit excellent thermal conductivity and Seebeck

coefficient, the performance is limited by electrical conductivity.

Table 4.2. Summary of thermoelectric performance of tumble ball milled materials compared to state of the art alternatives prepared using different methods. N-type $Bi_2Te_{2.7}Se_3$ prepared via planetary ball milling (Yan, 2010), P-type $Bi_{0.5}Sb_{1.5}Te_3$ prepared via wet chemistry (Hwang, 2012) and planetary ball milling (Poudel, 2008).

Property	$Bi_2Te_{2.7}Se_{0.3}$	[17]	$Bi_{0.5}Sb_{1.5}Te_3$	[37]	[3]
Temperature (K)	300	300	300	308	298
Charge Carrier Type	N-type	N-type	P-type	P-type	P-type
Electrical Conductivity (S/m)	9730	96500	18907	52500	125000
Seebeck Coefficient (μV/K)	173	189	243	248	187
Thermal Conductivity (W/m·K)	0.272	1.17	0.270	0.683	1.1
Figure of Merit	0.32	0.9	1.24	1.46	1.18

CHAPTER 5.   CONCLUSIONS AND FUTURE WORK

The use of tumble ball milling in order to create high-performance thermoelectric materials has been investigated for this work. Tumble ball milling is a potentially more cost-effective method of creating large amounts of nanoparticles than planetary ball milling or other synthesis methods. Through doping of Bi_2Te_3, thermoelectric materials with dimensionless figure of merits of 0.32 and 1.24 were created in n-type and p-type materials respectively. The use of graphene was also investigated as a method of improving thermoelectric performance in p-type materials, although more work is needed to draw conclusions on its efficacy.

The tumble ball milling process was optimized in order to eliminate contamination and maximize particle size reduction. It was found that tungsten carbide is a superior milling media due to its strength and hardness, which led to low contamination rates. Milling large amounts of media was found to eliminate contamination, especially when keeping the weight ratio of media to materials below 45:1. Materials milled using these methods for 3 days showed a particle size of 20 nm was achieved. Materials which have been ball milled and hot pressed show excellent thermal conductivities and Seebeck coefficients, but suffer from poor electrical conductivity.

If these materials are further investigated, work should be focused on the electrical properties of these materials. It is possible that graphene could improve these properties, but some more work on characterizing graphene samples is needed. Annealing of materials with graphene should also be investigated in order to discover if they benefit in the same ways that samples without graphene benefit

LIST OF REFERENCES

LIST OF REFERENCES

[1] Lawrence Livermore Nat. Lab., "Estimated U.S. energy use in 2011," https://flowcharts.llnl.gov/, Oct. 2012.

[2] Harman, T., Taylor, P., Walsh, M., and LaForge, B., 2002, "Quantum dot superlattice thermoelectric materials and devices," Science, 297(5590), pp. 2229-2232.

[3] Poudel, B., Hao, Q., Ma, Y., Lan, Y., Minnich, A., Yu, B., Yan, X., Wang, D., Muto, A., and Vashaee, D., 2008, "High-thermoelectric performance of nanostructured bismuth antimony telluride bulk alloys," Science, 320(5876), pp. 634-638.

[4] Fairbanks, J., 2011, "Automotive Thermoelectric Generators and HVAC," SAE 2011 Electronic Systems for Vehicle Propulsion Systems, Nov. 9, 2011.

[5] Friedensen, V. P., 1998, "Space nuclear power: Technology, policy, and risk considerations in human missions to Mars," Acta astronautica, 42(1), pp. 395-409.

[6] Rowe, D., and Min, G., 1996, "Design theory of thermoelectric modules for electrical power generation," IEE Proceedings-Science, Measurement and Technology, 143(6), pp. 351-356.

[7] Majumdar, A., and Reddy, P., 2004, "Role of electron–phonon coupling in thermal conductance of metal–nonmetal interfaces," Applied Physics Letters, 84(23), pp. 4768-4770.

[8] Hicks, L., and Dresselhaus, M., 1993, "Effect of quantum-well structures on the thermoelectric figure of merit," Physical Review B, 47(19), p. 12727.

[9] Hicks, L., and Dresselhaus, M., 1993, "Thermoelectric figure of merit of a one-dimensional conductor," Physical review B, 47(24), p. 16631.

[10] Hicks, L., Harman, T., Sun, X., and Dresselhaus, M., 1996, "Experimental study of the effect of quantum-well structures on the thermoelectric figure of merit," Physical Review B, 53(16), p. R10493.

[11] Zakeri, M., Allahkarami, M., Kavei, G., Khanmohammadian, A., and Rahimipour, M., 2009, "Synthesis of nanocrystalline Bi 2 Te 3 via mechanical alloying," journal of materials processing technology, 209(1), pp. 96-101.

[12] Scheele, M., Oeschler, N., Meier, K., Kornowski, A., Klinke, C., and Weller, H., 2009, "Synthesis and thermoelectric characterization of Bi2Te3 nanoparticles," Advanced Functional Materials, 19(21), pp. 3476-3483.

[13] Hulbert, D. M., Anders, A., Dudina, D. V., Andersson, J., Jiang, D., Unuvar, C., Anselmi-Tamburini, U., Lavernia, E. J., and Mukherjee, A. K., 2008, "The absence of plasma in "spark plasma sintering"," Journal of Applied Physics, 104(3), p. 033305.

[14] Yang, J., Fan, X., Chen, R., Zhu, W., Bao, S., and Duan, X., 2006, "Consolidation and thermoelectric properties of n-type bismuth telluride based materials by mechanical alloying and hot pressing," Journal of alloys and compounds, 416(1), pp. 270-273.

[15] Sponenburgh, L., 2006, "Ball milling theory and practice," Bridge City Enterprises, p.13.

[16] Deniz, V., and Onur, T., 2002, "Investigation of the breakage kinetics of pumice samples as dependent on powder filling in a ball mill," International journal of mineral processing, 67(1), pp. 71-78.

[17] Iwasaki, T., Yabuuchi, T., Nakagawa, H., and Watano, S., 2010, "Scale-up methodology for tumbling ball mill based on impact energy of grinding balls using discrete element analysis," Advanced Powder Technology, 21(6), pp. 623-629.

[18] Bernotat, S., and Schönert, K., 1988, "Size reduction," Ullmann's Encyclopedia of Industrial Chemistry.

[19] Yan, X., Poudel, B., Ma, Y., Liu, W., Joshi, G., Wang, H., Lan, Y., Wang, D., Chen, G., and Ren, Z., 2010, "Experimental studies on anisotropic thermoelectric properties and structures of n-type Bi2Te2. 7Se0. 3," Nano letters, 10(9), pp. 3373-3378.

[20] Humphry-Baker, S., and Schuh, C., 2014, "Anomalous grain refinement trends during mechanical milling of Bi 2 Te 3," Acta Materialia, 75, pp. 167-179.

[21] Liu, J., and Li, J. F., 2004, "Bi2Te3 and Bi2Te3/nano-SiC Prepared by Mechanical Alloying and Spark Plasma Sintering," Key Engineering Materials, 280, pp. 397-400.

[22] Oh, M., Son, J., Kim, B., Park, S., Min, B., and Lee, H., 2014, "Antisite defects in n-type Bi2 (Te, Se) 3: Experimental and theoretical studies," Journal of Applied Physics, 115(13), p. 133706.

[23] Son, J., Oh, M., Kim, B., Park, S., Min, B., Kim, M., and Lee, H., 2013, "Effect of ball milling time on the thermoelectric properties of p-type (Bi, Sb) 2 Te 3," Journal of Alloys and Compounds, 566, pp. 168-174.

[24] Brostow, W., Datashvili, T., Hagg Lobland, H. E., Hilbig, T., Su, L., Vinado, C., and White, J., 2012, "Bismuth telluride-based thermoelectric materials: Coatings as protection against thermal cycling effects," Journal of Materials Research, 27(22), pp. 2930-2936.

[25] Mio, H., Kano, J., and Saito, F., 2004, "Scale-up method of planetary ball mill," Chemical engineering science, 59(24), pp. 5909-5916.

[26] Watanabe, R., Hashimoto, H., and Lee, G. G., 1995, "Computer simulation of milling ball motion in mechanical alloying (overview)," Materials Transactions, JIM, 36(2), pp. 102-109.

[27] Patterson, A., 1939, "The Scherrer formula for X-ray particle size determination," Physical review, 56(10), p. 978.

[28] Baysinger, G., 2015, "CRC Handbook of Chemistry and Physics," National Institute of Standards and Technology, Section 12.

[29] http://www.ferroceramic.com/zirconia.htm

[30] https://www.ceramicindustry.com/ext/resources/pdfs/2013-CCD-Material-Charts.pdf

[31] Campbell, S. A., 2008, Fabrication engineering at the micro and nanoscale, Oxford University Press New York, p.45.

[32] Bando, H., Koizumi, K., Oikawa, Y., Daikohara, K., Kulbachinskii, V., and Ozaki, H., 2000, "The time-dependent process of oxidation of the surface of Bi2Te3 studied by x-ray photoelectron spectroscopy," Journal of Physics: Condensed Matter, 12(26), p. 5607.

[33] Teweldebrhan, D., Goyal, V., and Balandin, A. A., 2010, "Exfoliation and characterization of bismuth telluride atomic quintuples and quasi-two-dimensional crystals," Nano letters, 10(4), pp. 1209-1218.

[34] Teweldebrhan, D., Goyal, V., Rahman, M., and Balandin, A. A., 2010, "Atomically-thin crystalline films and ribbons of bismuth telluride," Applied Physics Letters, 96(5), pp. 053107-053107-053103.

[35] Churchill, S. W., and Chu, H. H., 1975, "Correlating equations for laminar and turbulent free convection from a horizontal cylinder," International Journal of Heat and Mass Transfer, 18(9), pp. 1049-1053.

[36] Kim, J. I., Lee, E. S., Kim, J. Y., Choi, S. M., Lee, K. H., and Seo, W. S., 2014, "Thermoelectric properties of unoxidized graphene/Bi2Te2. 7Se0. 3 composites synthesized by exfoliation/re-assembly method," physica status solidi (RRL)-Rapid Research Letters, 8(4), pp. 357-361.

[37] Hwang, S., Kim, S.-I., Ahn, K., Roh, J., Yang, D.-J., Lee, S.-M., and Lee, K.-H., 2013, "Enhancing the Thermoelectric Properties of p-Type Bulk Bi-Sb-Te Nanocomposites via Solution-Based Metal Nanoparticle Decoration," Journal of Electronic Materials, 42(7), pp. 1411-1416.

VITA

VITA

    Chris Robinson was born in Chesterton, IN. He graduated with a bachelor's degree in mechanical engineering from Purdue University in 2014 as part of a combined BS/MS program. He joined the Nanoscale Energy Transport and Conversion Laboratory in 2012 as an undergraduate student and has worked in the group ever since. Upon graduation, he will be moving to Boston, MA and looking for employment.

LIST OF PUBLICATIONS

LIST OF PUBLICATIONS

Chen, L., Rickey, K., Zhao, Q., Robinson, C., and Ruan, X., 2013, "Effects of nanocrystal shape and size on the temperature sensitivity in Raman thermometry," Applied Physics Letters, 103(8), p. 083107.